frontiers | Frontiers in Energy Research

TYPE Original Research
PUBLISHED 26 January 2026
DOI 10.3389/fenrg.2025.1764223

Check for updates

OPEN ACCESS

EDITED BY
Yu Jin,
Tianjin University, China

REVIEWED BY
Zhiping Dong,
City University of Hong Kong, Hong Kong SAR, China
Shunguang Lei,
Kunming University of Science and Technology, China

*CORRESPONDENCE
Pupu Chao,
chaopupu@dlut.edu.cn

RECEIVED 09 December 2025
REVISED 23 December 2025
ACCEPTED 30 December 2025
PUBLISHED 26 January 2026

CITATION
Jiang M, Shi S, Chao P, Zhang Z, She X, Ma K, Wang K, Zhang D and Li X (2026) Benchmark model of the DC sending-end system with high-penetration renewable energy for voltage stability analysis.
Front. Energy Res. 13:1764223.
doi: 10.3389/fenrg.2025.1764223

Benchmark model of the DC sending-end system with high-penetration renewable energy for voltage stability analysis

Minglei Jiang[1], Shengyao Shi[1], Pupu Chao[2]*, Zhipeng Zhang[1], Xin She[1], Kerui Ma[1], Kaiping Wang[1], Dachi Zhang[1] and Xin Li[1]

[1]Research Institute of Economics and Technology, State Grid Jilin Electric Power Company Limited, Changchun, China, [2]School of Electrical Engineering, Dalian University of Technology, Dalian, Liaoning, China

Introduction: With the increasing integration of renewable energy, the power grid is gradually facing multi-mode voltage stability problems, especially at the DC sending end. Thus, there is an urgent need to meet the voltage security and stability requirements of the DC sending-end power grid under different scenarios.

Methods: Based on the topology and operational data of an actual Chinese DC sending-end power grid, a high-penetration renewable-energy DC sending-end system was established using the Power System Analysis Synthesis Program. The system integrates 500 kV AC and ±800 kV DC networks, as well as renewable energy sources and synchronous generators. Typical multi-mode voltage stability scenarios, including transient overvoltage, low-high voltage interlocking, delayed voltage recovery and voltage collapse, were constructed under specific faults such as DC bipolar lockout and commutation failure. Key influencing factors of multi-mode voltage stability were systematically analyzed, including DC power output, the penetration of renewable energy, renewable energy control parameters, and the configuration of condenser.

Results: Simulation results indicate that the proposed model can well reflect the voltage stability characteristics under different scenarios and meet the requirements of voltage security and stability analysis for the high-penetration renewable energy DC transmission system.

Discussion: The established simplified model can serve as a basic platform for voltage stability analysis, providing a reliable foundation for subsequent related research on the voltage stability of DC sending-end power grids with high renewable energy penetration.

KEYWORDS

benchmark system, DC sending-end grid, delayed voltage recovery, high penetration of renewable energy, transient overvoltage

1 Introduction

With the 'Dual Carbon' goals, promoting energy transformation and the construction of a new-type power system have become important directions for the development of China's power industry. The installed capacity of renewable energy sources represented by wind power in the power grid has been continuously increasing (Jiang et al., 2022; Sun et al., 2022; Zhang and Kang, 2022). Meanwhile, to address the issue of power transmission from large-scale renewable energy bases in recent years, China has mainly adopted ultra-high voltage direct current (UHVDC) transmission lines, providing a solid guarantee for the efficient transmission of renewable energy power (Shi et al., 2022; Zhou et al., 2018).

However, in the DC sending-end system, as a large amount of renewable energy is connected to the grid, the grid's dynamic reactive power and voltage support capability has declined, and the problem of grid voltage stability has become increasingly prominent (Liu et al., 2020; Han et al., 2020; Zhou et al., 2022). At the same time, the interaction between renewable energy stations, the AC transmission grid, and DC has led to an increase in security and stability risks such as transient overvoltage and delayed voltage recovery, which have become the main factors restricting the consumption and transmission capacity of renewable energy (Han et al., 2024; Xin et al., 2019; Sun et al., 2021).

The benchmark system is the foundation for conducting power system research. Currently, in the context of the multi-form stability characteristics of the new-type power system with a high penetration of renewable energy, there are typical examples focusing on frequency and power angle stability issues (Wu et al., 2024; Xu et al., 2024; Li et al., 2023). Regarding the example systems for voltage stability with a high penetration of renewable energy, Li et al. (2023) focused on power angle and transient overvoltage issues and constructed a scenario where renewable energy and conventional power sources are bundled for transmission through AC and DC lines. Zhao et al. (2024) designed a DC receiving-end benchmark system that can reflect voltage collapse and sustained low voltage. The above-mentioned literature has constructed typical examples for the stability characteristics of the new-type power system, but there is still a lack of benchmark systems for the DC sending-end with a high penetration of renewable energy that can reflect multi-form voltage stability issues.

There are no typical benchmark systems for DC sending-end grids involving multi-form voltage stability issues. Existing studies mostly use the CIGRE HVDC as a standard example for analysis (Szechtman et al., 1991) and verify methods or strategies in actual power grids. Li et al. (2021) verified the effectiveness of the proposed measurement indicators for the transient overvoltage problem in the DC sending-end system in the CIGRE HVDC standard test system and actual DC sending-end systems. Ouyang et al. (2024) verified the control method of the rectifier station to suppress commutation failure overvoltage based on the CIGRE HVDC standard test model. Fu et al. (2016) analyzed the causes of delayed voltage recovery and the role of generators in the voltage recovery process and verified the optimization method in an actual power grid model. However, the examples currently used in research can only reflect some transient voltage issues in the system. Subsequent optimization and control strategy research based on these examples is difficult to take into account multi-form voltage stability issues. Moreover, the actual power grid model has a complex network structure and a large number of nodes, which can only be used for the verification of the effectiveness of theoretical methods and is difficult to support the mechanism analysis of transient voltage stability. In terms of multi-form voltage stability in high-penetration renewable energy DC sending-end grids, there is no example that can comprehensively reflect the transient voltage stability characteristics, and related optimization and strategy research work lacks an analysis and verification platform.

This paper addresses the multi-form voltage stability issues in high-penetration renewable energy DC sending-end systems. Based on the real-world grid configuration and data in China, a DC sending-end electromechanical transient benchmark system suitable for multi-form voltage stability analysis is established. The transmission grid is composed of 500 kV AC and ±800 kV UHVDC, and includes different types of power sources such as conventional energy, wind power, and photovoltaic power. Based on this benchmark, scenarios of overvoltage, low-high voltage interlocking, delayed voltage recovery, and voltage collapse with a high penetration of renewable energy are constructed, and the influence of factors, such as the penetration of renewable energy, renewable energy control parameters, DC transmission power, synchronous condenser configuration, and the proportion of induction motors on transient voltage stability, is analyzed. The results show that this benchmark can comprehensively reflect the impact of large-scale renewable energy access on the transient voltage of the DC sending-end system and can serve as a basic platform for voltage stability analysis and control strategy research.

2 Sending-end grid benchmark system with high penetration renewable energy

2.1 Systematic overview

Based on the topology and data of an actual DC sending-end power grid in a region of China, a simulation benchmark of a DC sending-end grid with a high penetration of renewable energy has been established using the Power System Analysis Synthesis Program (PSASP). The system primarily employs a 500 kV AC and ±800 kV DC grid, comprising 420 nodes at different voltage levels. The AC receiving-end network and the DC receiving-end network are respectively equivalent to infinite bus systems. The structure of the transmission grid is illustrated in Figure 1, and the node overview is summarized in Table 1. The UHVDC in the benchmark model is an ultra-high voltage DC based on line commutated converters (LCC-UHVDC). The converter stations adopt a bipolar structure, with each pole featuring a series connection of two 12-pulse converters. Specifically, the positive pole includes a positive pole high-voltage side converter and a positive pole low-voltage side converter, while the negative pole comprises a negative pole high-voltage side

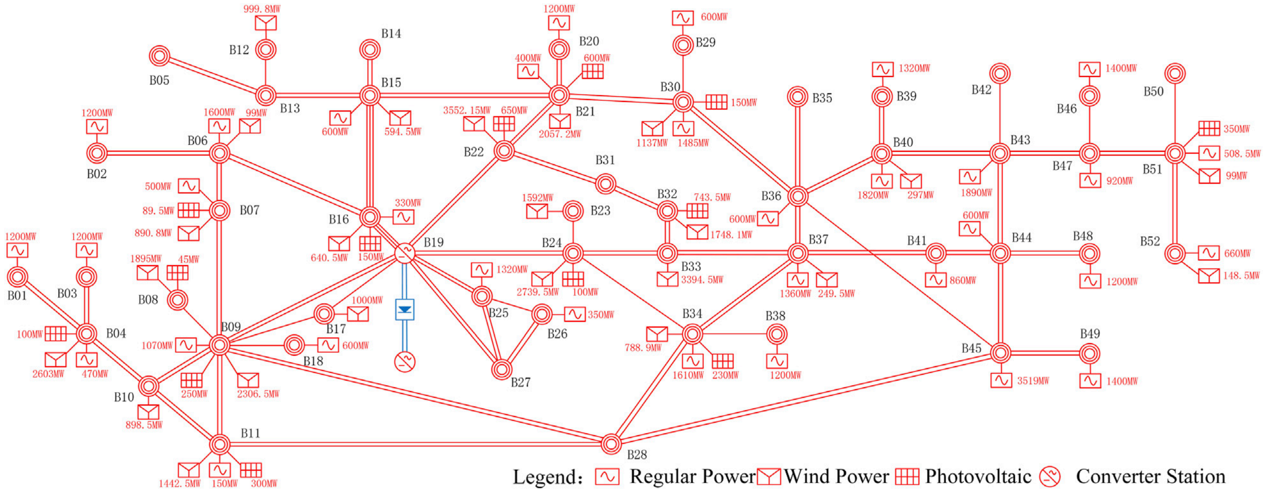

FIGURE 1
The transmission grid structure diagram of the power system.

TABLE 1 The overview of power system nodes.

Voltage level	Nodes	Notes
500 kV	54	AC transmission grid
220 kV	82	Load nodes,transformer nodes
Under 220 kV	284	Renewable, generator and capacitor nodes
Total	420	—

converter and a negative pole low-voltage side converter. Each converter is connected to the AC power grid through a converter transformer. The model structure of the UHVDC is shown in the Figure 2.

2.2 Lines and transformers overview

The system includes a total of 116 500 kV AC lines, 50 220 kV AC lines, 232 two-winding transformers, 38 three-winding transformers and one ±800 kV UHV DC transmission channel. The overview of the lines and transformers is shown in Table 2.

2.3 Power generation overview

The case study involves 134 thermal power units with an installed capacity of 35,142.5 MW; 51 renewable energy units of wind and photovoltaic power, with an installed capacity of 34,931.45 MW, including 31,173.45 MW of wind power and 3,758 MW of photovoltaic power. The penetration of renewable energy installed capacity is 49.85%. The overview of power source installed capacity is shown in Table 3.

In the simulation, the renewable energy installation at the renewable energy collection buses is summarized in Table 4.

2.4 Load and reactive power compensation overview

The system has a total active load of 14,346.07 MW and a total reactive load of 6,067.55 MVar, with the load evenly distributed throughout the system. In the renewable energy integration area, the loads are connected to the 220 kV buses and linked to the 500 kV buses via three-winding transformers. Reactive power compensation is provided by shunt capacitors and reactors. Specifically, the capacitor and reactor banks on the 500 kV lines are directly connected to the 500 kV buses, while those in the sub-500 kV network are connected to the low-voltage side buses of the three-winding transformers.

2.5 Basic system operating conditions

The basic operation mode of the system is shown in Table 5. The total output of conventional units in the system is 12,248 MW, the total output of renewable energy is 11,287.7 MW, the power transmitted through DC lines is 10,000 MW, and the penetration of renewable energy output is 47.96%.

3 Voltage stability characteristics of the sending-end power grid

A high-renewable-penetration DC sending-end power grid can exhibit multiple forms of voltage instability under different fault scenarios. Based on the established simulation system, various fault

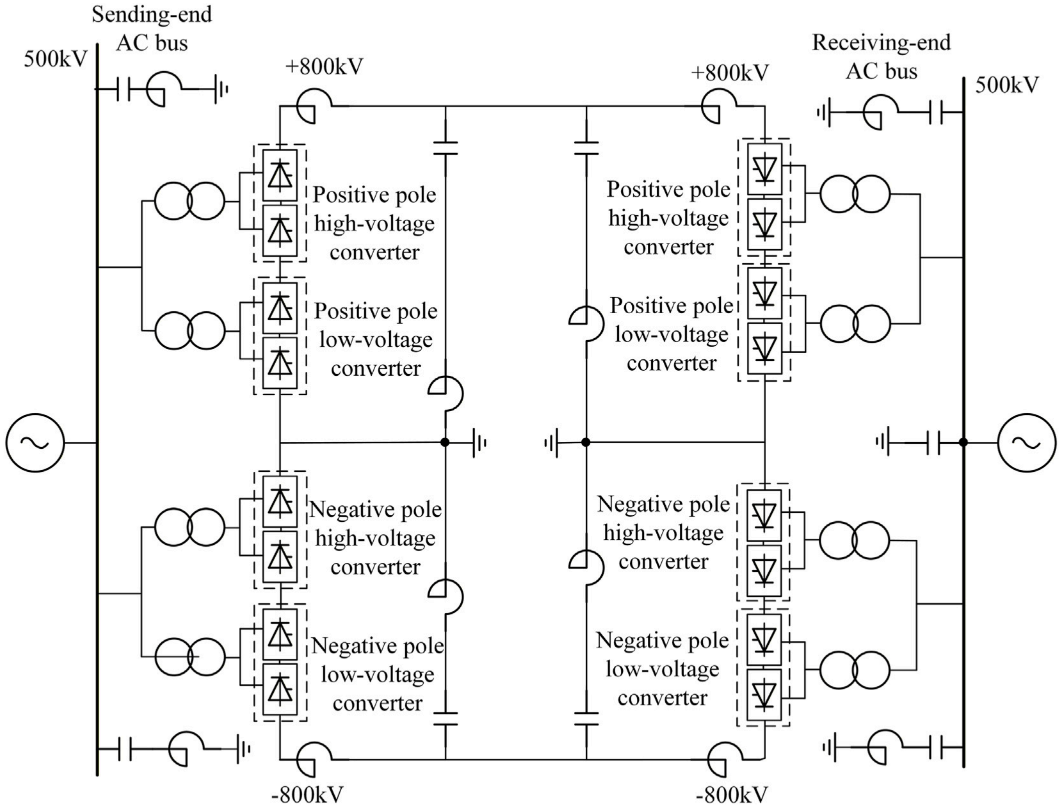

FIGURE 2
The model structure of the UHVDC.

scenarios were constructed to analyze the influencing factors of these diverse forms of voltage stability.

3.1 Transient overvoltage scenario

3.1.1 Transient overvoltage scenario construction

During operation, UHVDC converter stations consume a significant amount of reactive power. When a large disturbance occurs in the DC power, the reactive power balance between the converter station and the sending-end grid is disrupted, causing a large surplus of reactive power to flood into the DC sending-end system. This results in transient overvoltage in the DC sending-end system.

A bipolar lockout fault occurs in the UHVDC system at t = 1.0 s. The voltage at the sending-end converter bus rises, exhibiting transient overvoltage. The overvoltage state persists at the converter bus until the sending-end filter banks are tripped at t = 1.3 s. The voltage waveform at the sending-end converter bus is shown in Figure 3. The transient overvoltage at sending-end converter bus B19 reaches 1.42p.u., causing some renewable energy units in the vicinity of the DC link to trip due to overvoltage. The grid-connected terminal voltage and grid-connected power of some new energy sources are shown in Figures 4A,B respectively. Starting from 1.15 s, the grid-connected terminal voltage of some new energy sources in the DC near-area successively exceeds 1.3 p.u., and these new energy sources trip off the grid one after another, with their grid-connected power dropping to zero.

3.1.2 Analysis of influencing factors for transient overvoltage

The reactive power surplus at the DC sending-end during fault periods is the primary cause of transient overvoltage in the system. Among various quantitative analysis methods for transient overvoltage, the Single-Branch Voltage Drop Method is widely adopted due to its simultaneous consideration of active and reactive power variations. The calculation formula of this method is shown in Equation 1:

$$\Delta U = \frac{(P_0/S^2 - R)\Delta P + (Q_0/S^2 - X)\Delta Q}{U_N} \tag{1}$$

Where ΔU represents the voltage increment at the converter bus; U_N denotes the rated voltage of the converter bus; X and R are the equivalent reactance and resistance, respectively; ΔP and ΔQ indicate the active and reactive power variations in the sending-end AC system before and after the fault occurrence; P_0, and Q_0 are the initial active and reactive power values at the sending end under steady-state conditions, respectively; and S represents the short-circuit capacity of the converter station.

According to the formula, the overvoltage severity in the DC sending-end system is influenced by multiple factors, including the transmitted DC power and the configuration of synchronous

TABLE 2 The overview of lines and transformers.

Line type	Number	Notes	
AC Tie lines	166	500 kV AC grid	116
		220 kV low-voltage lines	50
Three-winding transformers	38	525/230/66 kV	27
		525/230/36 kV	3
		242/66/10.5 kV	8
Two-winding transformers	232	Conventional unit Step-up transformers	125
		Renewable energy unit transformers	50
		Renewable energy station Step-up transformers	50
DC line	1	Rated voltage	±800 kV
		Rated power	10000 MW

TABLE 3 The overview of power supply installation.

Unit type	Thermal	Renewable energy	
		Wind	PV
Capacity/MW	35,142.5	31,173.45	3,758

condensers at the sending end. Furthermore, considering the high concentration of renewable energy in the vicinity of the DC sending-end within the model, this section analyzes the overvoltage stability characteristics of the test system by varying the renewable energy penetration level, its control parameters, the transmitted DC power, and the synchronous condenser configuration.

3.1.2.1 Penetration of renewable energy

Under the basic operating condition, the committed capacity of renewable and thermal power units near the DC sending-end was modified while maintaining constant total generation output. Three scenarios with renewable energy penetration levels of 40%, 50%, and 60% at the DC sending-end were established. A bipolar lockout fault was applied at t = 1.0 s. The voltage response characteristics at the sending-end converter bus B19 under these conditions are shown in Figure 5.

The simulation results demonstrate that the transient overvoltage at the sending-end bus caused by the DC blocking fault increases significantly with the rise in renewable energy penetration level.

3.1.2.2 Renewable energy control parameters

When transient overvoltage occurs at the DC sending-end converter bus, a large number of renewable energy sources in the nearby collection area will enter a high-voltage ride-through (HVRT) state. Therefore, different HVRT control parameters result in varying reactive power responses from renewable energy during the fault, consequently affecting the transient overvoltage levels at nearby buses.

The reactive current control strategy during high-voltage ride-through (HVRT) for renewable energy often employs the specified current control method. The control formula for the reactive current component I_{qHV} is shown in Equation 2:

$$I_{\mathrm{qHV}} = K_{\mathrm{1q\_HV}}\left(V_{\mathrm{Hin}} - V_{\mathrm{t}}\right) + K_{\mathrm{2q\_HV}} I_{\mathrm{q0}} \tag{2}$$

Where $K_{\mathrm{1q\_HV}}$ is the HVRT reactive current calculation coefficient 1, $K_{\mathrm{2q\_HV}}$ is the HVRT reactive current calculation coefficient 2, V_{Hin} is the HVRT entry threshold voltage, V_{t} is the terminal voltage magnitude, and I_{q0} is the initial reactive current. Since the initial reactive current I_{q0} is small and close to zero, the influence of $K_{\mathrm{2q\_HV}}$ on the voltage during HVRT can be neglected. Therefore, the analysis primarily focuses on the impact of the calculation coefficient 1 $K_{\mathrm{1q\_HV}}$ on the overvoltage.

Under the base operating condition, the first HVRT reactive current calculation coefficient, $K_{\mathrm{1q\_HV}}$, was configured to values of 1, 1.5, and 2 respectively. A bipolar lockout fault was applied to the DC system at t = 1.0 s. The voltage response characteristics at the sending-end converter bus B19 are shown in Figure 6.

The simulation results show that the higher the renewable energy HVRT reactive current calculation coefficient 1 $K_{\mathrm{1q\_HV}}$, the lower the overvoltage at the system's sending-end bus.

3.1.2.3 DC transmitted power

Based on the base operating condition, the DC transmitted power was reduced while the sending-end filter banks were adjusted. Scenarios with DC transmitted power levels of 10,000 MW, 9,000 MW, and 8,000 MW were established. A bipolar lockout fault was applied at t = 1.0 s. The voltage response characteristics at the sending-end converter bus B19 are shown in Figure 7.

TABLE 4 The installed capacity overview of the renewable energy convergence bus power supply at the DC sending-end grid.

Bus	Conventional/MW	RE installation/MW		RE share
		Wind	PV	
B04	470	2,603	100	85.2%
B06	1,600	99	0	5.8%
B07	500	890.8	89.5	66.2%
B08	0	1895	45	100.0%
B09	1,070	2,306.5	250	70.5%
B10	0	898.5	0	100.0%
B11	150	1,442.5	300	92.1%
B12	0	999.8	0	100.0%
B15	600	594.5	0	49.8%
B16	330	640.5	150	70.5%
B17	0	1,000	0	100.0%
B21	400	2057.2	600	86.9%
B22	0	3,552.15	650	100.0%
B23	0	1,592	0	100.0%
B24	0	2,739.5	100	100.0%
B30	1,485	1,137	150	46.4%
B32	0	1748.1	743.5	100.0%
B33	0	3,394.5	0	100.0%
B34	1,610	788.9	230	38.8%
B37	1,360	249.5	0	15.5%
B40	1820	297	0	14.0%
B51	508.5	99	350	46.9%
B52	660	148.5	0	18.4%

TABLE 5 The basic operating mode of the condition system.

Power/MW		Load/MW	DC Export/MW	AC interface/MW	Loss/MW
Conventional/MW	RE/MW				
12,248	11,287.7	15,320.5	10,000	2,234.46	1,410.66

The simulation results show that the higher the DC transmitted power, the more severe the transient overvoltage at both the sending-end converter bus and the nearby renewable generator terminal buses during a fault.

3.1.2.4 Synchronous condenser configuration

Synchronous condensers, as a common type of dynamic reactive power compensation equipment, can enhance system voltage stability and are widely used in DC sending-end systems. Under

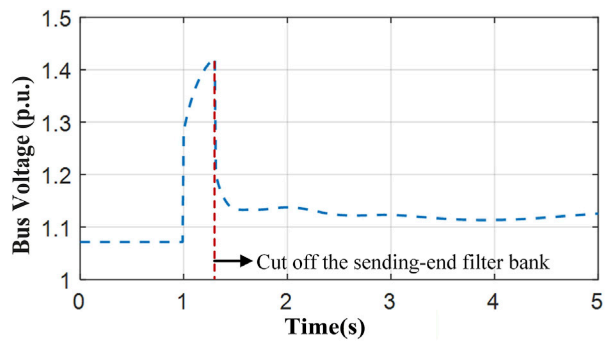

FIGURE 3
Transient overvoltage after bipolar blocking fault.

the base operating condition, two additional comparative cases were established by configuring one and two synchronous condensers, respectively, each with a rated capacity of 300 MVA, at the DC sending-end converter bus B19. A bipolar lockout fault was applied at t = 1.0 s. The voltage response characteristics at the sending-end converter bus B19 are shown in Figure 8.

The simulation results demonstrate that the installation of synchronous condensers can mitigate transient overvoltage during bipolar lockout faults. Furthermore, a higher total configured capacity of synchronous condensers results in lower transient overvoltage levels at the DC sending-end converter bus. In this paper, "SC" is the abbreviation for Synchronous Condenser.

In summary, a higher renewable energy penetration level, a smaller HVRT reactive current coefficient 1 K_{1q_HV}, a greater DC transmitted power, along with a lower configured capacity of synchronous condensers in the DC sending-end system will collectively lead to more severe transient overvoltage at the sending-end bus caused by DC block faults.

3.2 Low-high voltage cascade scenario

3.2.1 Low-high voltage cascade scenario construction

Commutation failure is one of the most common faults in conventional UHVDC transmission systems. When a fault occurs in the receiving-end grid, it can affect the commutation voltage of the thyristors in the DC converter station, leading to commutation failure in the inverter.

Under the base operating condition, a DC commutation failure fault is set to occur at t = 1.0 s. At the onset of commutation failure, the inverter side reduces its firing angle to improve the commutation margin. As the firing angle increases, the DC voltage at the receiving end drops rapidly, and the DC current rises sharply. This causes an increase in the firing angle of the sending-end converter, leading to higher reactive power absorption from the AC grid by the sending-end converter station. Consequently, the voltage at the sending-end converter bus decreases initially during the early stage of the fault. Subsequently, under the regulation of the Voltage Dependent Current Order Limiter (VDCOL), the DC current decreases rapidly, reducing the reactive power consumption at the sending end. The resulting significant surplus of reactive power at the sending end induces transient overvoltage at the sending-end converter bus, as shown in Figure 9.

3.2.2 Analysis of influencing factors for the low-high voltage cascade

The impacts of various influencing factors including the penetration of renewable energy, renewable energy control parameters, DC transmission power, and synchronous condenser configuration on low-high voltage interlocking have been analyzed respectively. The impacts of the influencing factors on low-high voltage interlocking are illustrated in Figure 10. A detailed analysis is conducted in the subsequent sections.

3.2.2.1 Penetration of renewable energy

Based on the base operating condition and while maintaining constant total system power, three operational scenarios were configured by modifying the renewable energy penetration level at the DC sending-end to 40%, 50%, and 60% respectively. The system was subsequently set to experience a DC commutation failure fault at t = 1.0 s. The voltage response characteristics at the sending-end converter bus B19 are shown in Figure 10A.

The simulation results indicate that as the renewable energy penetration level increases during a DC commutation failure fault, the severity of the transient low voltage at the sending-end converter bus decreases, while the degree of transient over-voltage remains largely unchanged. This suggests that the renewable energy penetration level does not have a significant impact on a single DC commutation failure event.

3.2.2.2 Renewable energy control parameters

Under the base operating condition, the first renewable energy HVRT reactive current calculation coefficient, K_{1q_HV}, was configured to values of 0, 0.5, and 1 respectively. A DC commutation failure fault was applied to the system at t = 1.0 s. The voltage response characteristics at the sending-end converter bus B19 are shown in Figure 10B.

The simulation results demonstrate that the transient overvoltage at the sending-end bus progressively decreases as the renewable energy HVRT reactive current calculation coefficient 1 K_{1q_HV} increases.

The reactive current control strategy during low-voltage ride-through (LVRT) for renewable energy often employs the specified current control method. The formula for the reactive current component I_{qLV} during LVRT is shown in Equation 3.

$$I_{qLV} = K_{1q\_LV}\left(V_{Lin} - V_t\right) + K_{2q\_LV} I_{q0} \tag{3}$$

In the formula, K_{1q_LV} is the LVRT reactive current calculation coefficient 1, K_{2q_LV} is the LVRT reactive current calculation coefficient 2, and V_{Lin} is the LVRT entry threshold voltage. Since the initial reactive current I_{q0} during steady-state operation of renewable energy is small and essentially zero, adjusting the LVRT reactive current calculation coefficient 2 K_{2q_LV} has a negligible impact on the voltage during LVRT. Therefore, the analysis primarily focuses on the effect of the calculation coefficient K_{1q_LV} on the low-voltage response.

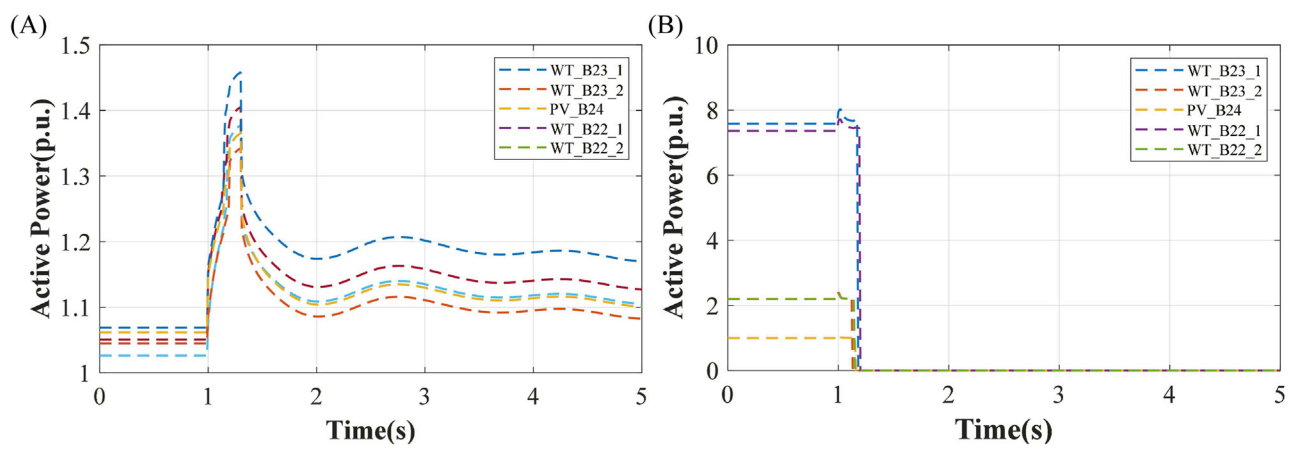

FIGURE 4
The grid-connected terminal voltage and grid-connected power of some new energy sources. **(A)** The grid-connected terminal voltage of some new energy sources. **(B)** The grid-connected power of some new energy sources.

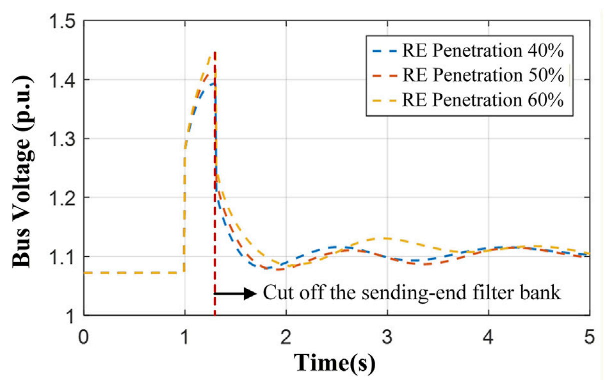

FIGURE 5
Transient overvoltage curve under different penetrations of renewable energy.

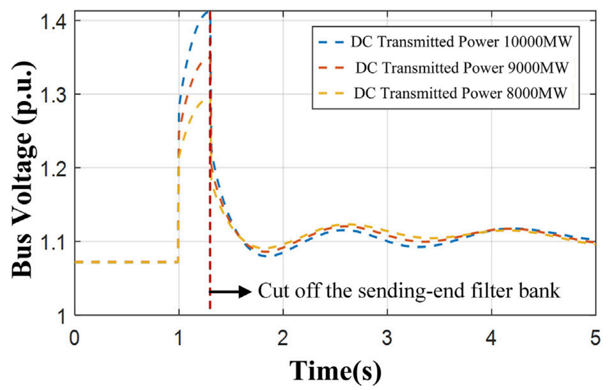

FIGURE 7
Transient overvoltage curve under different DC output power.

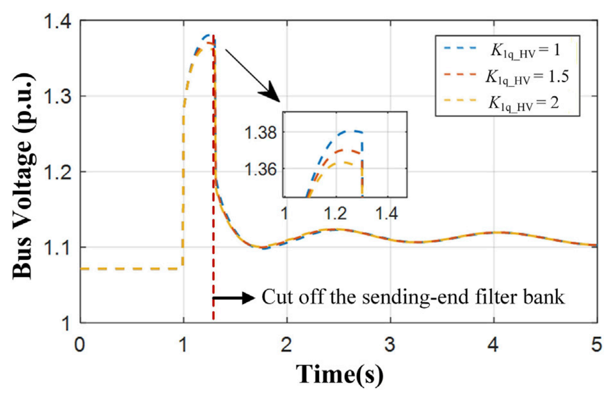

FIGURE 6
Transient overvoltage curve under different values of the first HVRT reactive current calculation coefficient (K_{1q_HV}).

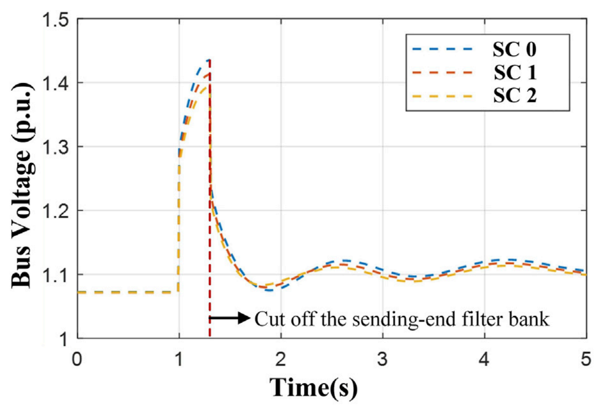

FIGURE 8
Transient overvoltage curves under different synchronous condensers.

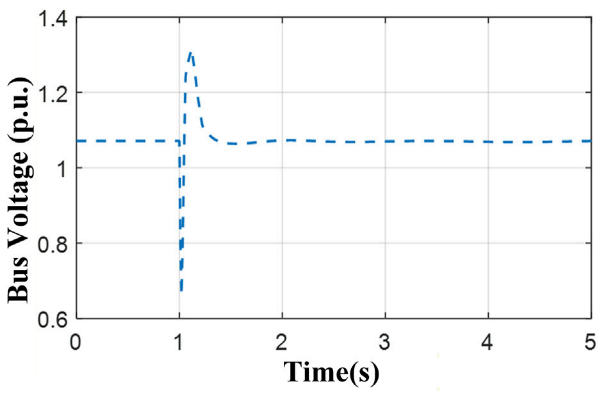

FIGURE 9
Low- and high-voltage interlock after DC single commutation failure.

Under the base operating condition, the first LVRT reactive current calculation coefficient, K_{1q_LV}, was set to 0.5, 1, and 1.5, respectively. A DC commutation failure fault was applied to the system at t = 1.0 s. The voltage response characteristics at the sending-end converter bus B19 are shown in Figure 10C.

The simulation results indicate that as the renewable energy LVRT reactive current calculation coefficient 1 K_{1q_LV} increases, the low-voltage level at the sending-end bus caused by commutation failure becomes less severe, while the overvoltage severity increases.

3.2.2.3 DC transmission power

Based on the base operating condition and while maintaining constant total power delivery through both AC and DC transmission channels, scenarios with DC transmitted power levels of 10,000 MW, 9,000 MW, and 8,000 MW were established. A DC commutation failure fault was applied to the system at t = 1.0 s. The voltage response characteristics at the sending-end converter bus B19 are shown in Figure 10D.

The simulation results indicate that as the DC transmitted power increases, the transient low voltage at the sending-end converter bus during the fault decreases, while the transient overvoltage increases. Specifically, at DC transmitted power levels of 10,000 MW, 9,000 MW, and 8,000 MW, the transient low voltages caused by a single commutation failure are 0.662 p.u., 0.676 p.u., and 0.692 p.u., respectively, while the corresponding transient overvoltage values are 1.314 p.u., 1.266 p.u., and 1.223 p.u.

3.2.2.4 Synchronous condenser configuration

Based on the base operating condition, the DC sending-end converter bus B19 was configured with zero, one, and two synchronous condensers respectively, each with a rated capacity of 300 MVA. A DC commutation failure fault was applied to the system at t = 1.0 s. The voltage response characteristics at the DC sending-end converter bus B19 are shown in Figure 10E.

The simulation results demonstrate that configuring synchronous condensers can improve the transient low voltage and suppress the transient overvoltage during DC commutation failure events.

In summary, a higher renewable energy penetration level at the DC sending-end results in less severe transient low voltage during commutation failure events; a smaller HVRT reactive current calculation coefficient 1, K_{1q_HV}, leads to higher transient overvoltage; a smaller LVRT reactive current calculation coefficient 1, K_{1q_LV}, reduces both transient low voltage and overvoltage; while greater DC transmitted power and lower synchronous condenser capacity exacerbate both transient low voltage and overvoltage conditions.

3.3 Delayed voltage recovery scenario

3.3.1 Voltage delayed recovery scenario construction

Under the base operating condition, the power sources and load overview for Bus B34 are summarized in Table 6. The load model comprises 40% static load, 30% unstable motor load, and 30% stable motor load.

A three-phase short-circuit ground fault occurred at the 220 kV load bus under Node B34 at t = 1.0 s, causing the regional voltage to rapidly drop to a very low level. The induction motors within the load began absorbing reactive power from the system. At t = 1.5 s, after fault clearance, the induction motors became unstable and continued to draw a significant amount of reactive power, preventing the system voltage from recovering to its normal level. The voltage waveforms of some nodes under Bus B34 are shown in Figure 11. Following the clearance of the short-circuit fault, the load bus voltage failed to recover normally, resulting in the terminal voltage of the wind turbines remaining below 0.9 p.u., thereby reducing the system's voltage stability.

3.3.2 Analysis of influencing factors for delayed voltage recovery

The impacts of various influencing factors including the committed capacity of thermal power, proportion of unstable induction motors, renewable energy control parameter, and synchronous condenser configuration on delayed voltage recovery have been analyzed respectively. Delayed voltage recovery characteristics at renewable energy terminal buses under various influencing factors are illustrated in Figure 12. A detailed analysis is conducted in the subsequent sections.

3.3.2.1 Committed capacity of thermal power

Based on the base operating condition, the committed thermal power capacity connected to Bus B34 was adjusted to 100 MW, 200 MW, and 300 MW, respectively. A three-phase short-circuit fault was applied at the 220 kV load bus under Node B34 at t = 1.0 s. The voltage waveforms at the renewable energy terminal buses under Bus B34 are shown in Figure 12A.

The simulation results indicate that a higher committed capacity of thermal power near the renewable energy generation area supplies more reactive power during voltage dips, making the system less prone to delayed voltage recovery.

3.3.2.2 Proportion of unstable induction motors

Under the base operating condition, the proportion of unstable induction motors in the load was adjusted to 20%, 30%, and 40%,

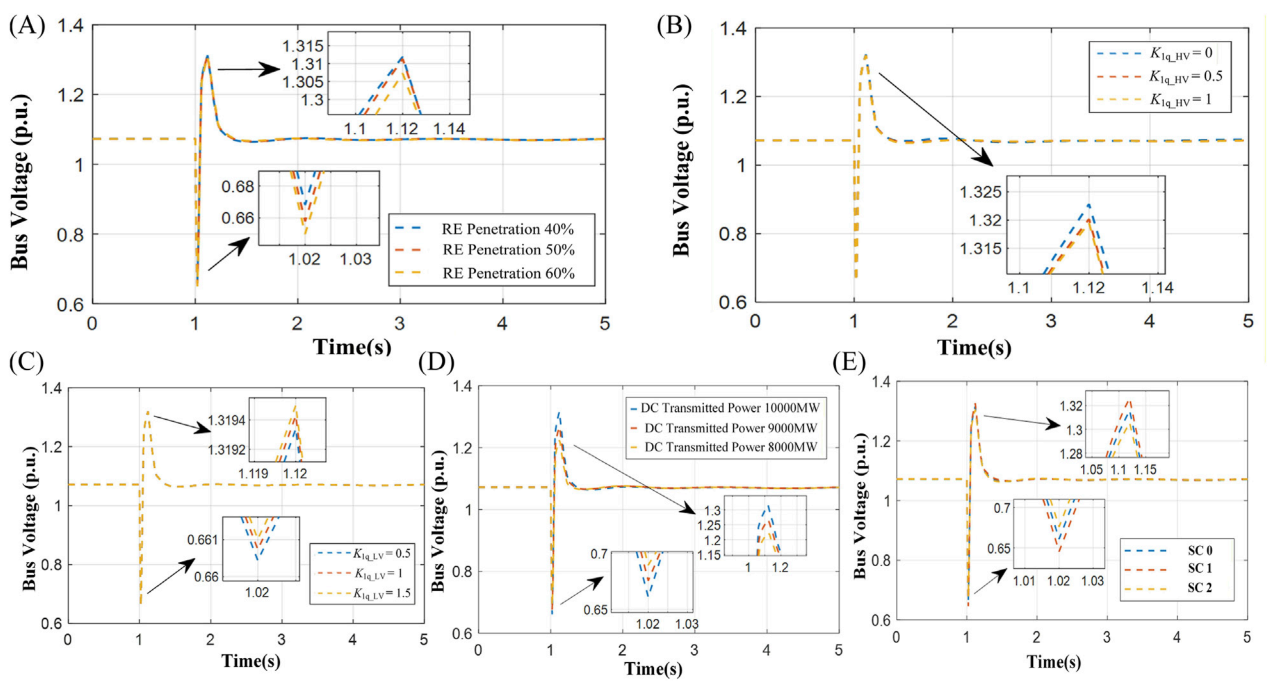

FIGURE 10
The impacts of the influencing factors on low-high voltage interlocking. **(A)** Low- and high-voltage interlocking curve under different penetrations of renewable energy. **(B)** Low- and high-voltage interlocking curve under different values of the first HVRT reactive current calculation coefficient (K_{1q_HV}). **(C)** Low- and high-voltage interlocking curve under different values of the first LVRT reactive current calculation coefficient (K_{1q_LV}). **(D)** Low- and high-voltage interlocking curve under different DC output power. **(E)** Low- and high-voltage interlocking curve under different synchronous condensers.

TABLE 6 The overview of power supply and load under B34 bus.

Generation/MW			Load absorption	
Conventional/MW	Doubly-Fed/MW	Direct-Drive/MW	Active Power/MW	Reactive Power/MVar
100	598.9	147	1,015.47	212.903

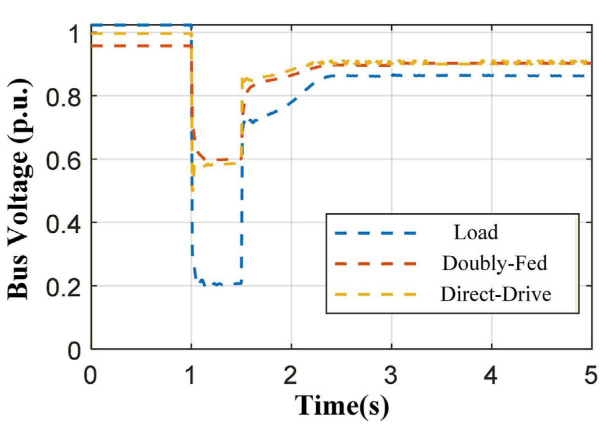

FIGURE 11
Delayed voltage recovery after a fault.

respectively. A three-phase short-circuit fault was applied at the 220 kV load bus under Node B34 at $t = 1.0$ s. The voltage waveforms at the renewable energy terminal buses under Bus B34 are shown in Figure 12B.

The simulation results indicate that a higher proportion of unstable induction motors leads to increased reactive power absorption by the motor load after a three-phase short-circuit fault, resulting in lower voltage at the load bus, decreased voltage at the renewable energy terminal bus, and a higher likelihood of delayed voltage recovery.

3.3.2.3 Renewable energy control parameter

Under the base operating condition, the first LVRT reactive current calculation coefficient, K_{1q_LV}, was set to 0.5, 1, and 1.5, respectively. A three-phase short-circuit fault was applied at the 220 kV load bus under Node B34 at $t = 1.0$ s. The voltage

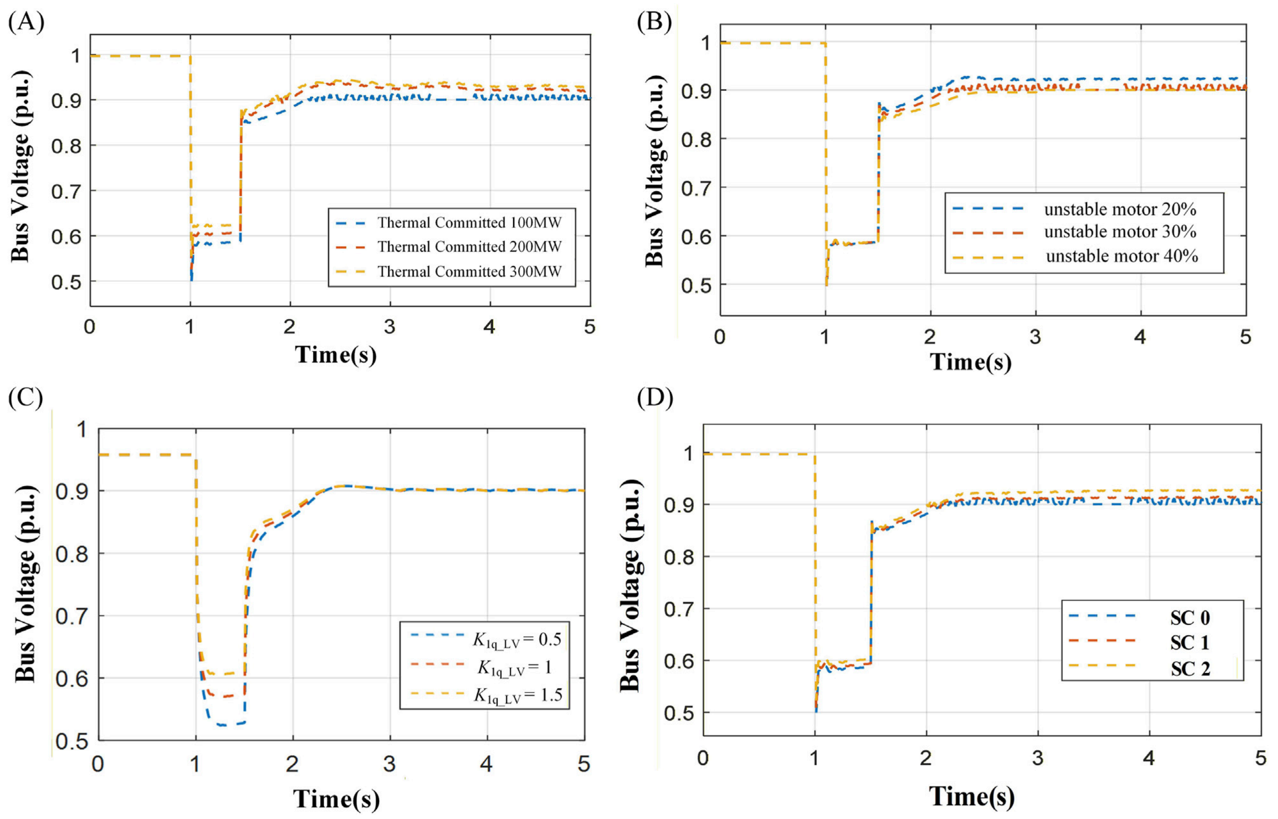

FIGURE 12
Delayed voltage recovery characteristics at renewable energy terminal buses under various influencing factors. **(A)** Effect of the committed capacity of nearby thermal power. **(B)** Effect of the proportion of unstable induction motors in the load. **(C)** Effect of different values of the first LVRT reactive current calculation coefficient (K_{1q_LV}). **(D)** Effect of the configured capacity of synchronous condensers.

waveforms at the renewable energy terminal buses under Bus B34 are shown in Figure 12C.

The simulation results indicate that a larger LVRT reactive current calculation coefficient 1 K_{1q_LV} leads to a higher reactive current component during the fault, resulting in a less severe voltage dip. However, K_{1q_LV} has minimal impact on delayed voltage recovery.

3.3.2.4 Synchronous condenser configuration

Under the base operating condition, one and two synchronous condensers with a rated capacity of 50 MVA were configured at the 220 kV bus under Bus B34, forming two additional comparative cases. Subsequently, a three-phase short-circuit fault was applied at the 220 kV load bus under Node B34 at t = 1.0 s. The voltage waveforms at the renewable energy terminal buses under Bus B34 are shown in Figure 12D.

The simulation results demonstrate that the greater the configured capacity of synchronous condensers, the more reactive power is supplied during a voltage dip, making the system less susceptible to delayed voltage recovery.

In summary, the lower the committed thermal power capacity near the renewable energy area, the higher the proportion of unstable induction motors, and the less the configured capacity of synchronous condensers, the more severe the delayed voltage recovery phenomenon at the renewable energy terminal buses; while the LVRT reactive current calculation coefficient 1 K_{1q_LV} has minimal impact on delayed voltage recovery.

3.4 Voltage collapse scenario

A voltage collapse scenario has been established, and the impacts of various influencing factors including the penetration of renewable energy, DC transmission power, and synchronous condenser configuration on voltage collapse have been analyzed respectively. The analysis of the influencing factors under the voltage collapse scenario is illustrated in Figure 13. A detailed analysis is conducted in the subsequent sections.

3.4.1 Voltage collapse scenario construction

On the basis of the basic operating condition, the proportion of renewable energy and the total system power are kept unchanged. At t = 1.0 s, a three-phase permanent short-circuit fault occurs on one circuit of the double-circuit line between B09 and B10, near the B09 side. Subsequently, at t = 1.2 s, the double-circuit line is tripped. After the line is removed, voltage collapse occurs at buses B04, B10, B01, and B03, as shown in Figure 13A.

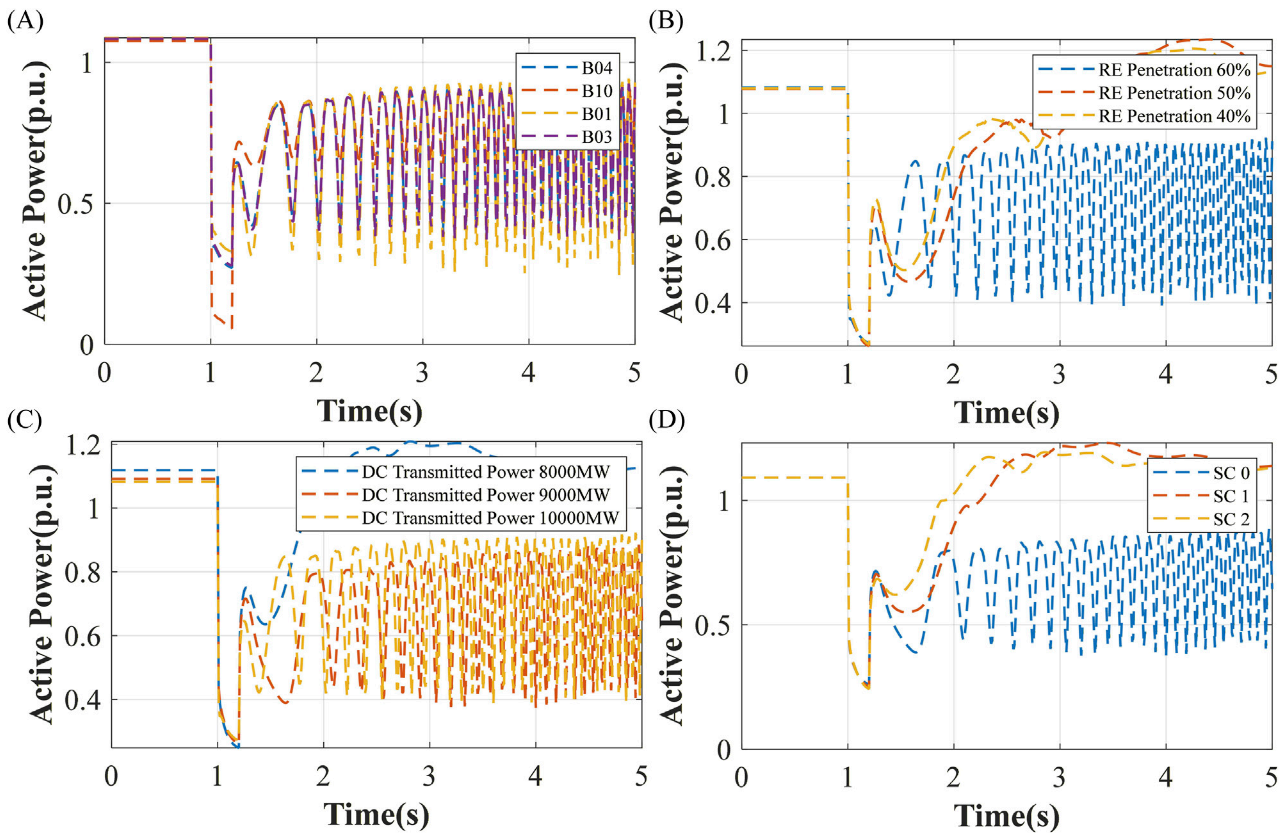

FIGURE 13
The analysis of the influencing factors under the voltage collapse scenario. **(A)** Voltage collapse curve after the AC fault. **(B)** Bus voltage of bus B04 under different penetrations of renewable energy. **(C)** Bus voltage of bus B04 under different DC output power. **(D)** Bus voltage of bus B04 under different synchronous condensers.

3.4.2 Analysis of influencing factors for voltage collapse

3.4.2.1 Penetration of renewable energy

On the basis of the basic operating condition, while keeping the total system power unchanged, three scenarios are formed by adjusting the proportion of renewable energy at the DC sending end to 40%, 50%, and 60%, respectively. At t = 1.0 s, a three-phase permanent short-circuit fault occurs on one circuit of the double-circuit line between B09 and B10, near the B09 side. Subsequently, at t = 1.2 s, the double-circuit line is tripped. The voltage waveform of bus B04 after the AC fault is shown in Figure 13B.

Simulation results indicate that the greater the proportion of renewable energy generation at the DC sending end, the more severe the voltage collapse after fault clearance, and that the share of renewable energy generation significantly impacts voltage collapse.

3.4.2.2 DC transmission power

On the basis of the basic operating condition, while keeping the total power of the AC and DC outgoing transmission channels unchanged, three scenarios are formed by adjusting the DC sending power to 10,000 MW, 9000 MW, and 8000 MW, respectively. At t = 1.0 s, a three-phase permanent short-circuit fault occurs on one circuit of the double-circuit line between B09 and B10, near the B09 side. Subsequently, at t = 1.2 s, the double-circuit line is tripped. The voltage waveform of bus B04 after the AC fault is shown in Figure 13C.

Simulation results indicate that the greater the DC sending power, the more severe the voltage collapse after fault clearance, and the DC sending power significantly impacts the voltage collapse.

3.4.2.3 Synchronous condenser configuration

On the basis of the basic operating condition, one and two synchronous condensers with a rated capacity of 50 MVA each are configured on the 220 kV bus under Bus B34, forming two new comparative scenarios. At t = 1.0 s, a three-phase permanent short-circuit fault occurs on one circuit of the double-circuit line between B09 and B10, near the B09 side. Subsequently, at t = 1.2 s, the double-circuit line is tripped. The voltage waveform of bus B04 after the AC fault is shown in Figure 13D.

Simulation results show that synchronous condensers provide voltage support after fault clearance. The more capacity of synchronous condensers configured, the less likely voltage collapse occurs after fault clearance.

In summary, a higher share of renewable energy generation, greater DC sending power, and a smaller capacity of synchronous condensers configured will make the renewable energy generator terminal voltage more susceptible to triggering voltage collapse after AC fault clearance.

Conclusion

This paper addresses the modeling requirements for studying multi-form voltage stability in DC sending-end grids with high penetration of renewable energy. Based on real-world grid operational conditions, a simplified model of a DC sending-end grid suitable for electromechanical transient voltage stability analysis was developed. This test system effectively captures the multi-form voltage stability issues prevalent in DC sending-end grids with high renewable penetration in China, demonstrating various stability phenomena under different operating conditions, including transient overvoltage, low-high voltage cascades, delayed voltage recovery, and voltage collapse. Through analysis using this test system, the influencing factors of multi-form voltage stability were investigated. The results show that higher renewable penetration levels, greater DC transmitted power, and fewer synchronous condenser configurations not only exacerbate both transient low-voltage and overvoltage conditions but also increase the likelihood of voltage collapse. Additionally, less committed thermal power capacity near renewable energy areas, a higher proportion of unstable induction motors, and lower synchronous condenser capacity increase the likelihood of delayed voltage recovery at renewable energy terminals. While adjusting the key reactive current injection coefficients during HVRT and LVRT (K_{1q_HV}, K_{1q_LV}) can alleviate transient low-voltage and overvoltage issues, they have minimal impact on delayed voltage recovery. This test system can effectively support research on multi-form voltage stability characteristics and control strategies for DC sending-end systems with high renewable energy penetration.

Data availability statement

The original contributions presented in the study are included in the article/supplementary material, further inquiries can be directed to the corresponding author.

Author contributions

MJ: Writing – original draft, Resources, Funding acquisition, Conceptualization, Project administration, Supervision. SS: Formal Analysis, Writing – original draft, Validation, Methodology. PC: Conceptualization, Writing – original draft, Formal Analysis. ZZ: Data curation, Investigation, Writing – review and editing, Formal Analysis. XS: Formal Analysis, Writing – review and editing. KM: Methodology, Writing – review and editing, Validation, Data curation. KW: Visualization, Writing – review and editing, Data curation, Validation. DZ: Visualization, Writing – review and editing. XL: Writing – review and editing, Data curation, Visualization.

Funding

The author(s) declared that financial support was received for this work and/or its publication. This work was supported by the Science and Technology Project of State Grid Corporation of China (Grant No. SGJLJY00GPJS2400041) and the Strategic Consulting Project of Jilin Provincial Department of Science and Technology (Grant No. JL2023-09).

Acknowledgements

The authors gratefully acknowledge the State Grid Jilin Electric Power Company Limited for providing the grid operational data and technical support essential to this study. We also thank our research team members for their insightful discussions and collaboration.

Conflict of interest

Authors MJ, SS, ZZ, XS, KM, KW, DZ, and XL were employed by State Grid Jilin Electric Power Company Limited.

The remaining author(s) declared that this work was conducted in the absence of any commercial or financial relationships that could be construed as a potential conflict of interest.

Generative AI statement

The author(s) declared that generative AI was not used in the creation of this manuscript.

Any alternative text (alt text) provided alongside figures in this article has been generated by Frontiers with the support of artificial intelligence and reasonable efforts have been made to ensure accuracy, including review by the authors wherever possible. If you identify any issues, please contact us.

Publisher's note

References

Fu, C., Sun, W., and Li, X. M. (2016). Dynamic voltage/reactive power sensitivity method for improving delayed voltage recovery in power grids. *Proc. CSU-EPSA* 28 (10), 42–46+54. doi:10.3969/j.issn.1003-8930.2016.10.008

Han, T., Li, B. J., Zhang, Z. Y., Niu, S. B., Ke, X. B., Huo, C., et al. (2020). Research on security and stability defense system for weak sending-end power grid with wind-solar-thermal bundling and multi-DC. *Electr. Power Eng. Technol.* 39 (03), 15–22. doi:10.12158/j.2096-3203.2020.03.003

Han, L., Yin, C. Y., Dai, C., and Ma, X. (2024). Transient voltage operation risk analysis of sending-end system with high proportion of renewable energy. *Power Syst. Prot. Control* 52 (01), 23–34. doi:10.19783/j.cnki.pspc.230311

Jiang, H. L., Liu, Y. Q., Feng, Y. M., Zhou, B. Z., and Li, Y. X. (2022). Analysis of power generation technology trends during the "14th Five-Year Plan" period under the background of carbon peak and carbon neutrality. *Power Gener. Technol.* 43 (1), 54–64. doi:10.12096/j.2096-4528.pgt.21030

Li, X. Y., Li, F. T., Yin, C. Y., and Bai, H. B. (2021). Calculation method of transient overvoltage in sending-end system under DC bipolar blocking fault. *Power Syst. Prot. Control* 49 (01), 1–8. doi:10.19783/j.cnki.pspc.200214

Li, M. J., Guo, Q., He, J. B., Li, W. F., Liu, M. S., Sun, H. Y., et al. (2023). Typical example system of UHV AC/DC system with high proportion of renewable energy (part I): example system for voltage and rotor angle stability. *Power Syst. Technol.* 47 (10), 3935–3943. doi:10.13335/j.1000-3673.pst.2022.2341

Liu, Z. X., You, P. Y., and Zhou, Q. Y. (2020). Review on transmission technology for wide-area accommodation of high-proportion renewable energy systems. *Electr. Power Eng. Technol.* 39 (05), 59–70. doi:10.12158/j.2096-3203.2020.05.009

Ouyang, J. X., Tao, R., Pan, X. Y., Xiao, C., Guo, C. Y., Pang, M. Y., et al. (2024). Control method for AC transient overvoltage at sending end of HVDC transmission system based on unbalanced reactive power and trigger angle error compensation. *Power Syst. Prot. Control* 52 (24), 53–63. doi:10.19783/j.cnki.pspc.240384

Shi, W. H., Qu, J. X., Luo, K., Li, Q. M., He, Y. J., Wang, W. S., et al. (2022). Research on the development of high-proportion renewable energy grid integration and operation. *Strategic Study CAE* 24 (06), 52–63. doi:10.15302/J-SSCAE-2022.07.006

Sun, D. W., Wu, L. L., Liu, H., Song, P., Li, Y. H., Wang, X., et al. (2021). Low voltage ride-through characteristics of direct-drive permanent magnet synchronous generator in weak grid and its impact on terminal transient voltage. *Proc. CSEE* 41 (14), 4777–4786. doi:10.13334/j.0258-8013.pcsee.201078

Sun, H. D., Xu, S. Y., Xu, T., Bi, J. T., Zhao, B., Guo, Q., et al. (2022). Analysis on definition and classification of power system security and stability. *Proc. CSEE* 42 (21), 7796–7809. doi:10.13334/j.0258-8013.pcsee.221846

Szechtman, M., Wess, T., and Thio, C. V. (1991). "A benchmark model for HVDC system studies," in International Conference on AC and DC Power Transmission (London, UK: IET), 374–378.

Wu, P., Zhao, B., Cheng, Y., and Sun, H. D. (2024). Standard test system for new power systems (Part II): Frequency stability CSEE-FS. *Proc. CSEE* 44 (19), 7531–7543. doi:10.13334/j.0258-8013.pcsee.230533

Xin, J. B., Wang, Y. L., Shu, Z., Chen, B., and Cheng, S. M. (2019). Impact analysis of UHV AC/DC integration on transient stability of Jiangxi power grid. *Power Syst. Prot. Control* 47 (08), 71–79. doi:10.7667/PSPC180558

Xu, S. Y., Li, Z. H., Zhao, B., and Sun, H. D. (2024). Standard test system for new power systems (part I): rotor angle stability CSEE-RAS. *Proc. CSEE* 44 (15), 5973–5985. doi:10.13334/j.0258-8013.pcsee.230534

Zhang, Z. G., and Kang, C. Q. (2022). Challenges and prospects of constructing new power systems under the goal of carbon neutrality. *Proc. CSEE* 42 (8), 2806–2819. doi:10.13334/j.0258-8013.pcsee.220467

Zhao, B., Xu, S. Y., Lan, T. K., and Sun, H. D. (2024). Standard test system for new power systems (Part III): voltage stability CSEE-VS. *Proc. CSEE* 44 (21), 8353–8364. doi:10.13334/j.0258-8013.pcsee.230536

Zhou, X. X., Chen, S. Y., Lu, Z. X., Huang, Y. H., Ma, S. C., Zhao, Q., et al. (2018). Technical characteristics of China's new generation power system in energy transition. *Proc. CSEE* 38 (7), 1893–1904+2205. doi:10.13334/j.0258-8013.pcsee.180067

Zhou, Y. K., Xie, H., Sun, H. D., Xu, S. Y., Zhao, B., Zhang, Y., et al. (2022). Influence of low voltage ride-through control parameters of renewable energy units on power frequency overvoltage at generator terminals. *Power Syst. Technol.* 46 (5), 1907–1916. doi:10.13335/j.1000-3673.pst.2021.0871